Research Square

Preprints are preliminary reports that have not undergone peer review.
They should not be considered conclusive, used to inform clinical practice,
or referenced by the media as validated information.

Receiver-Dependent Harmonic Selection Near Time-Modulated Dielectric Slabs Revealed by Three-Dimensional Dyadic Green's Functions

Abdorreza Torabi

ab.reza.torabi@ut.ac.ir

University of Tehran

Somayeh Dolatkhah Takloo

K. N. Toosi University of Technology

Article

Keywords:

Posted Date: November 26th, 2026

DOI: https://doi.org/10.21203/rs.3.rs-11700839/v1

License: This work is licensed under a Creative Commons Attribution 4.0 International License.
Read Full License

Additional Declarations: No competing interests reported.

Receiver-Dependent Harmonic Selection Near Time-Modulated Dielectric Slabs Revealed by Three-Dimensional Dyadic Green's Functions

Abdorreza Torabi*
School of Engineering Science, College of Engineering, University of Tehran, Tehran, Iran
Somayeh Dolatkhah Takloo
Department of Electrical Engineering, K.N. Toosi University of Technology, Tehran, Iran
Somayeh.dolatkhah@email.kntu.ac.ir

Abstract

A nonperturbative Floquet–Nyström formulation is used to reconstruct the scattered three-dimensional electric-current dyadic of an exterior point source above a finite-thickness, laterally infinite time-modulated dielectric slab. Coupled TE/TM spectral equations retain the longitudinal contact term, and outgoing Fourier–Bessel inversion supplies five independent complex Cartesian entries. Analytical Fresnel limits, axial Maxwell finite differences, continuous-depth transfer, and a four-method benchmark provide bounded accuracy tests. At a common 0.1% full-dyadic error threshold, Nyström is accurate but is not the fastest tested solver; first Born fails in the examined stronger-modulation regime. The validated dyadic additionally predicts receiver-conditioned harmonic selection: a +27.74-dB second-to-first sideband contrast reverses to -30.44 dB upon moving the receiver, owing to vector-component interference. Signed-frequency dipole tests corroborate source–pump–radiation power balance. These findings demonstrate a reproducible, polarization-resolved source–receiver characterization, not exclusive numerical superiority or a global pump-stability certificate.

Keywords: Dyadic Green function, time-modulated dielectric, Floquet scattering, point dipole, transverse-electric/transverse-magnetic waves, Maxwell finite differences, radiation power, Sommerfeld integrals.

1 Introduction

Time-periodic dielectrics exchange energy with an external modulation pump and couple fields at frequencies $\omega_n = \omega_0 + n\Omega$. Reviews of time-varying photonics, active spatiotemporal metasurfaces, and nonstationary electromagnetic models emphasize both the opportunities for frequency conversion and the importance of material dispersion and causal modeling [1–4]. Photonic time crystals can exhibit momentum gaps and temporal-interface phenomena [5, 6]; temporal reflection and broadband frequency translation have also been experimentally observed [7]. These observations motivate rigorous Floquet modeling, but a homogeneous temporal interface or time-crystal band structure does not itself supply the scattered source-to-receiver dyadic of a finite-thickness layer.

Time-dependent planar structures have a substantial prior literature. Space–time-gradient metasurfaces were introduced for nonreciprocal wave manipulation [8], and a traveling-wave-modulated dielectric slab was analyzed as a nonreciprocal harmonic generator and quasisonic isolator [9]. For temporally modulated slabs, an equivalent-circuit treatment explicitly addressed parametric instability [10]; a later Floquet-matrix formulation incorporated dispersion and

*Corresponding author: ab.reza.torabi@ut.ac.ir

dissipation into the spectral operator [11]. The present model is instead a scalar, instantaneous, purely time-periodic dielectric slab, and neither the analysis nor the numerical tests below constitute a general stability or realistic dispersive-material certificate.

A prescribed incident Floquet channel can be treated by a scattering or transfer matrix. A localized three-dimensional current source requires considerably more: its complete transverse-wave-number spectrum, outgoing Sommerfeld inversion, the correct electric-current normalization and contact term, and a Cartesian dyadic that can be projected onto an arbitrary receiver polarization. Dyadic Green representations and singular/contact contributions for *static* layered Maxwell media are well established [12, 13]. Kreiczer and Hadad developed a Green-function theory for spatiotemporally modulated wire surfaces [14], while Kreiczer, Steinberg, and Hadad analyzed a *two-dimensional* localized source above a temporally modulated dielectric half-space [15]. Wapenaar and Slob considered three-dimensional Green and propagator matrices in spatially homogeneous time-varying materials [16]. Thus neither Floquet Green functions nor Sommerfeld transforms are claimed as new in isolation.

Harmonic beam manipulation and joint frequency–spatial control have also been developed with digital space–time-coding metasurfaces [17], rapidly switched meta-atoms [18], and experimentally demonstrated nonreciprocal space–time phase modulation [19]. Simultaneous frequency/polarization conversion, engineered harmonic energy allocation, and narrow frequency selectivity have subsequently been reported [20–22]. These devices usually target prescribed illumination, metasurface coding, or nonreciprocal functionality; the present paper does not claim to discover harmonic steering, polarization conversion, or frequency mixing.

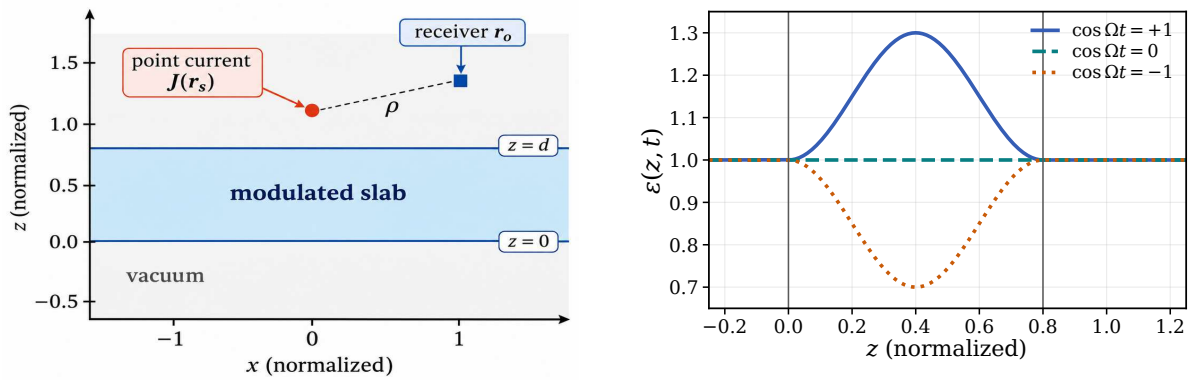
Antenna and dipole radiation provides a particularly relevant second line of comparison. A time-periodic patch-antenna substrate has been used for harmonic engineering through a cavity model [23]; time-varying Mie resonators have been studied for directional emitter-radiation control using Floquet multipoles [24]; and dispersive photonic time crystals have been analyzed for broadband dipole absorption and emission dynamics [25]. Sustaeta-Osuna *et al.* investigated near-field gain and far-field dipole control at a *dispersive plasmonic* time-crystal slab [26]. These results establish strong prior art for source-controlled harmonic radiation, but differ in geometry, constitutive response, antenna loading, or the computed observable from the scattered three-dimensional *electric-current* dyadic considered here.

More directly related mathematical constraints include the pseudounitary Floquet scattering formulation of Globosits, Hüpfl, and Rotter [27], quasinormal-mode and open-Floquet resonance analyses [28–30], and generalized slab/sphere/metasurface Floquet scattering [31]. These studies delimit what can legitimately be called a new contribution: we claim neither a new Floquet conservation law, universal numerical superiority, nor priority for dipole-induced harmonic conversion.

The objective here is instead a *specific, reproducible computational and physical characterization*: the scattered electric-current dyadic of an exterior three-dimensional point source above a laterally unbounded, finite-thickness, instantaneously time-modulated slab. A nonperturbative volume-integral Floquet–Nyström construction retains TE/TM channels and the longitudinal contact contribution, producing five independent complex Cartesian entries after outgoing Fourier–Bessel inversion. We (i) test the result against analytical Fresnel limits, independent axial Maxwell finite differences, and continuously profiled transfer solutions; (ii) compare the full dyadic with sliced transfer, an independent Chebyshev Maxwell Green boundary-value solver, and first Born using a common vector-error threshold, wall time, memory, and multiple-query reconstruction; and (iii) use the checked dyadic for receiver-projected harmonic observables, including a quantitative spatial reversal of sideband selectivity caused by vector-component interference. Signed-frequency physical-dipole tests further provide angular far-field cuts, hemispherically integrated harmonic powers, and source–pump–radiation balance as consistency controls, not new conservation theorems.

The paper follows this progression from formulation to numerical checks and physical inference. Section 2 defines the source-normalized dyadic and receiver projection, Section 3 defines signed-

frequency and radiative observables, and Section 4 presents accuracy, four-method benchmarks, source–receiver selectivity, and dipole radiation. The simulations assume a real instantaneous scalar dielectric and finite Floquet truncation; the independent FDFD checks are transverse-spectral (2.5-D), not full Cartesian three-dimensional Maxwell tests, and global pump/pole stability and realistic material dispersion remain unverified.



(a) (b)

Figure 1: (a) Conceptual geometry of the exterior point-current source $\mathbf{J}(\mathbf{r}_s)$ and receiver $\mathbf{r}_o$ above a laterally infinite dielectric slab occupying $0 < z < d$, with lateral source–receiver offset ρ. (b) Representative snapshots of the material law $\varepsilon(z,t) = 1 + \alpha \sin^2(\pi z/d)\cos(\Omega t)$ for $\alpha = 0.3$ at three modulation phases. The physical slab is finite in thickness but infinite in lateral extent.

2 Mathematical Formulation

2.1 Geometry, material law, and normalization

As depicted in Fig. 1(a), consider a nonmagnetic, infinite planar dielectric layer $0 < z < d$ embedded in vacuum, with a point electric-current source at $\boldsymbol{r}_s = (0, 0, z_s)$ and a receiver at $\boldsymbol{r}_o = (\rho, 0, z_o)$, where $z_s, z_o > d$. We use normalized units $\varepsilon_0 = \mu_0 = c_0 = 1$ and the $\mathrm{e}^{-\mathrm{i}\omega t}$ convention throughout. The constitutive response is assumed isotropic, local, instantaneous, and real:

$$\varepsilon(z,t) = 1 + f(z)\big[\Delta\varepsilon_s + \alpha\cos(\Omega t)\big], \quad \mu(z,t) = 1, \tag{1}$$

with $f(z) = \sin^2(\pi z/d)$ in the modulated tests, $f = 0$ outside the layer, and $f \equiv 1$ for the independent static Fresnel verification. Here α is the modulation depth and $\Delta\varepsilon_s$ the stationary contrast. We require $\varepsilon(z,t) > 0$ and a well-posed, stable scattering solution in the parameter regimes actually tested. Equation (1) is a deliberately idealized instantaneous law, not a microscopic causal dispersion model. The chosen periodic modulation permits a Floquet representation but is not an arbitrary aperiodic two-time Green function.

The electromagnetic source is a *current* dipole, not an electric dipole moment:

$$\boldsymbol{J}(\boldsymbol{r},t) = \boldsymbol{p}\,\delta(\boldsymbol{r} - \boldsymbol{r}_s)\mathrm{e}^{-\mathrm{i}\omega_0 t}, \quad \boldsymbol{p} \in \{\hat{\boldsymbol{x}}, \hat{\boldsymbol{y}}, \hat{\boldsymbol{z}}\}. \tag{2}$$

A point electric dipole moment $\boldsymbol{p}_{\mathrm{dip}}$ corresponds instead to $\boldsymbol{J} = -\mathrm{i}\omega_0 \boldsymbol{p}_{\mathrm{dip}}\delta(\boldsymbol{r} - \boldsymbol{r}_s)$; this distinction fixes the dimensional prefactor. With $\omega_n = \omega_0 + n\Omega$, $-N \le n \le N$, write $\boldsymbol{E}(\boldsymbol{r},t) = \sum_n \boldsymbol{E}_n(\boldsymbol{r})\mathrm{e}^{-\mathrm{i}\omega_n t}$ and similarly for $\boldsymbol{H}$. The primary positive-frequency dyadic inversion uses $\omega_0 - N\Omega > 0$; a separate signed-frequency Maxwell transfer formulation is introduced below for physical consistency checks. Neither truncation represents a general causal dispersive Green theory [32].

2.2 Maxwell–Floquet equations and a physically normalized dyadic

The Maxwell equations, written harmonic by harmonic using the stated time convention, are

$$\nabla \times \boldsymbol{E}_n = \mathrm{i}\omega_n \boldsymbol{H}_n, \tag{3}$$

$$\nabla \times \boldsymbol{H}_n = \boldsymbol{J}_n - \mathrm{i}\omega_n \sum_m \varepsilon_{nm}(z)\boldsymbol{E}_m, \tag{4}$$

where the Toeplitz convolution matrix is

$$\varepsilon_{nm}(z) = \delta_{nm} + f(z)\left[\Delta\varepsilon_s \delta_{nm} + \frac{\alpha}{2}(\delta_{n,m+1} + \delta_{n,m-1})\right]. \tag{5}$$

Eliminating $\boldsymbol{H}_n$ gives, without a Born approximation,

$$\left(\nabla \times \nabla \times -\omega_n^2\right)\boldsymbol{E}_n = \mathrm{i}\omega_n \boldsymbol{J}_n + \omega_n^2 \sum_m \Delta\varepsilon_{nm}(z)\boldsymbol{E}_m, \tag{6}$$

where $\Delta\varepsilon_{nm} = \varepsilon_{nm} - \delta_{nm}$. The sideband coupling on the right is essential: replacing ω_n^2 with ω_m^2 would describe a different material model.

Take the transverse Fourier transform $\widehat{u}(\boldsymbol{k}_\parallel, z) = \int_{\mathbb{R}^2} u(\boldsymbol{\rho}, z)\mathrm{e}^{-\mathrm{i}\boldsymbol{k}_\parallel\cdot\boldsymbol{\rho}}\mathrm{d}^2\boldsymbol{\rho}$ with $\kappa = |\boldsymbol{k}_\parallel|$. For the positive real frequencies used here, define the retarded outgoing branch

$$q_n(\kappa) = \sqrt{\omega_n^2 - \kappa^2 + \mathrm{i}0}, \qquad g_n(z, z') = \frac{\mathrm{i}\mathrm{e}^{\mathrm{i}q_n|z-z'|}}{2q_n}, \tag{7}$$

where $q_n > 0$ below the light line and $\operatorname{Im} q_n > 0$ for evanescent transverse spectra. Then $(\partial_z^2 + q_n^2)g_n = -\delta(z - z')$. Let $(\hat{\boldsymbol{e}}_\kappa, \hat{\boldsymbol{e}}_s, \hat{\boldsymbol{z}})$ be the local orthonormal basis, where $\hat{\boldsymbol{e}}_s = \hat{\boldsymbol{z}} \times \hat{\boldsymbol{e}}_\kappa$. The vacuum electric resolvent is

$$\mathsf{G}^{(0)}_{ss,n} = g_n, \qquad \mathsf{G}^{(0)}_{\kappa\kappa,n} = \frac{q_n^2}{\omega_n^2} g_n, \tag{8}$$

$$\mathsf{G}^{(0)}_{\kappa z,n} = \mathsf{G}^{(0)}_{z\kappa,n} = \frac{\mathrm{i}\kappa}{\omega_n^2}\partial_z g_n, \qquad \mathsf{G}^{(0)}_{zz,n} = \frac{\kappa^2}{\omega_n^2} g_n - \frac{\delta(z - z')}{\omega_n^2}.$$

Proposition 1 (Longitudinal contact and correct point-current normalization)**.** *The diagonal distribution in* (8) *is necessary for the full Maxwell inverse, and the incident field inside the layer is* $\widehat{\boldsymbol{E}}_n^{\mathrm{inc}}(z) = \delta_{n0}\mathrm{i}\omega_0 \mathsf{G}_0^{(0)}(z, z_s)\boldsymbol{p}$.

Proof. The scalar outgoing Green function satisfies $\partial_z^2 g_n = -q_n^2 g_n - \delta(z - z')$. Therefore $(1 + \omega_n^{-2}\partial_z^2)g_n = (\kappa^2/\omega_n^2)g_n - \delta/\omega_n^2$, giving exactly $\mathsf{G}^{(0)}_{zz,n}$ in (8). Inverting the vacuum operator $\nabla\times\nabla\times-\omega_0^2$ in (6) multiplies the point-current source by $\mathrm{i}\omega_0$, fixing the stated source normalization. Since $z_s > d$, the source distribution does not intersect the slab discretization; only its exact incident Weyl trace enters the volume solve. □

2.3 Nonperturbative volume-integral system

The spectral Dyson/Lippmann–Schwinger equation for the total electric field inside the slab is

$$\widehat{\boldsymbol{E}}_n(z) = \widehat{\boldsymbol{E}}_n^{\mathrm{inc}}(z) + \omega_n^2 \sum_m \int_0^d \mathsf{G}_n^{(0)}(z, z')\Delta\varepsilon_{nm}(z')\widehat{\boldsymbol{E}}_m(z')\mathrm{d}z'. \tag{9}$$

The scattered field observed in vacuum obeys

$$\widehat{\boldsymbol{E}}_n^{\mathrm{sc}}(z_o) = \omega_n^2 \sum_m \int_0^d \mathsf{G}_n^{(0)}(z_o, z')\Delta\varepsilon_{nm}(z')\widehat{\boldsymbol{E}}_m(z')\mathrm{d}z'. \tag{10}$$

The kernel within (9) includes the zz contact term, while (10) has no contact contribution for $z_o > d$. The isotropic planar geometry separates one s-polarized TE channel and one coupled (κ, z) TM block, each containing all retained Floquet harmonics. Upon finite depth discretization and harmonic truncation, (9) becomes

$$\mathsf{M}_{N,N_z}(\kappa)\boldsymbol{e} = \boldsymbol{b}, \qquad \mathsf{G}^{\mathrm{sc}}_{N,N_z} = \mathsf{C}\mathsf{M}^{-1}_{N,N_z}\mathsf{B}. \tag{11}$$

When the matrix is nonsingular, the inverse includes arbitrarily repeated harmonic interactions *within this finite model*, rather than stopping at first Born order. This is a known resolvent principle, not an assertion of a new integral-equation theorem.

For N_z equal cells $h = d/N_z$ with centers z_j, the off-diagonal free-space cell-integrated kernel and its diagonal limit are respectively

$$\begin{aligned} K^{(n)}_{ij} &= \frac{\mathrm{i}h}{2q_n}\,\mathrm{sinc}\!\left(\frac{q_n h}{2}\right)\mathrm{e}^{\mathrm{i}q_n|z_i - z_j|}, \quad i \neq j, \\ K^{(n)}_{ii} &= \frac{\mathrm{e}^{\mathrm{i}q_n h/2} - 1}{q_n^2}, \qquad \partial_{z_i} K^{(n)}_{ii} = 0, \end{aligned} \tag{12}$$

where $\mathrm{sinc}(x) = \sin x/x$. The local $-\delta/\omega_n^2$ term is assembled separately in the TM self-block.

2.4 Azimuthal reconstruction of the three-dimensional dyadic

For $\boldsymbol{\rho}_o - \boldsymbol{\rho}_s = (\rho, 0)$, let the local scattered response matrix to three unit current sources have nonzero entries $S_n = G^{\mathrm{sc}}_{ss,n0}$, $P_n = G^{\mathrm{sc}}_{\kappa\kappa,n0}$, $X_n = G^{\mathrm{sc}}_{\kappa z,n0}$, $Y_n = G^{\mathrm{sc}}_{z\kappa,n0}$, $Z_n = G^{\mathrm{sc}}_{zz,n0}$, with $J_l = J_l(\kappa\rho)$. Direct azimuthal integration gives

$$\begin{aligned} G^{\mathrm{sc}}_{xx,n0} &= \frac{1}{4\pi}\int_0^\infty \kappa[(S_n + P_n)J_0 + (S_n - P_n)J_2]\mathrm{d}\kappa, \\ G^{\mathrm{sc}}_{yy,n0} &= \frac{1}{4\pi}\int_0^\infty \kappa[(S_n + P_n)J_0 - (S_n - P_n)J_2]\mathrm{d}\kappa, \\ G^{\mathrm{sc}}_{xz,n0} &= \frac{\mathrm{i}}{2\pi}\int_0^\infty \kappa X_n J_1 \mathrm{d}\kappa, \quad G^{\mathrm{sc}}_{zx,n0} = \frac{\mathrm{i}}{2\pi}\int_0^\infty \kappa Y_n J_1 \mathrm{d}\kappa, \\ G^{\mathrm{sc}}_{zz,n0} &= \frac{1}{2\pi}\int_0^\infty \kappa Z_n J_0 \mathrm{d}\kappa. \end{aligned} \tag{13}$$

Here $G_{xy} = G_{yz} = 0$ by mirror symmetry in the source/receiver plane; they are not assumed to vanish for arbitrary observation azimuth.

Angular identities. At fixed κ, $(\hat{\boldsymbol{e}}_\kappa)_x = \cos\theta$ and $(\hat{\boldsymbol{e}}_s)_x = -\sin\theta$. In the Fourier inverse $\int_0^{2\pi} \mathrm{e}^{\mathrm{i}\kappa\rho\cos\theta}(\cdot)\mathrm{d}\theta$, use $\int \mathrm{e}^{\mathrm{i}x\cos\theta}\mathrm{d}\theta = 2\pi J_0(x)$, $\int \mathrm{e}^{\mathrm{i}x\cos\theta}\cos\theta\mathrm{d}\theta = 2\pi\mathrm{i}J_1(x)$, and $\int \mathrm{e}^{\mathrm{i}x\cos\theta}\cos(2\theta)\mathrm{d}\theta = -2\pi J_2(x)$. Taking $\cos^2\theta = (1 + \cos 2\theta)/2$ and $\sin^2\theta = (1 - \cos 2\theta)/2$, with the overall Fourier factor $(2\pi)^{-2}$, yields (13). □

The reconstructed quantity is a point-source *three-dimensional scattered electric-current dyadic*, not a general causal two-time fundamental solution. The total carrier field is $\mathsf{G}^{\mathrm{tot}}_{n0} = \mathsf{G}^{\mathrm{sc}}_{n0} + \delta_{n0}\mathrm{i}\omega_0\mathsf{G}^{(0)}_0$ with the appropriate free-space Fourier inversion.

2.5 Independent transverse-spectral Maxwell boundary-value formulation

For a numerical test independent of the volume-integral discretization, we solve the *differential* Maxwell–Floquet equations by a finite-volume frequency-domain finite-difference (FDFD) method with exact vacuum Dirichlet-to-Neumann (DtN) radiation conditions in each transverse spatial

channel. Introduce $\boldsymbol{\omega} = \mathrm{diag}(\omega_{-N}, \dots, \omega_N)$, $\boldsymbol{Q} = \mathrm{diag}(q_{-N}, \dots, q_N)$, and the Toeplitz matrix $\boldsymbol{\varepsilon}(z) = [\varepsilon_{nm}(z)]$. The TE field vector $\boldsymbol{u}^{\mathrm{TE}} = [E_{s,n}]$ satisfies inside the slab

$$\frac{\mathrm{d}^2 \boldsymbol{u}^{\mathrm{TE}}}{\mathrm{d}z^2} + [\boldsymbol{\omega}^2 \boldsymbol{\varepsilon}(z) - \kappa^2 \mathbf{I}] \boldsymbol{u}^{\mathrm{TE}} = 0. \tag{14}$$

For TM, use $\boldsymbol{h} = [H_{s,n}]$ and the tangential electric vector $\boldsymbol{e}_\kappa = [E_{\kappa,n}]$; source-free Maxwell equations inside the slab give

$$\begin{aligned} \boldsymbol{h}' &= \mathrm{i}\boldsymbol{\omega}\boldsymbol{\varepsilon}\, \boldsymbol{e}_\kappa, \\ \boldsymbol{e}_\kappa' &= \mathrm{i}\boldsymbol{\omega}\boldsymbol{h} - \mathrm{i}\kappa^2 \boldsymbol{\varepsilon}^{-1}\boldsymbol{\omega}^{-1}\boldsymbol{h}. \end{aligned} \tag{15}$$

Consequently, with $\mathsf{A}(z) = \boldsymbol{\varepsilon}(z)^{-1}\boldsymbol{\omega}^{-1}$,

$$\frac{\mathrm{d}}{\mathrm{d}z}\big[\mathsf{A}(z)\boldsymbol{h}'\big] + [\boldsymbol{\omega} - \kappa^2 \mathsf{A}(z)]\boldsymbol{h} = 0. \tag{16}$$

Proposition 2 (Equivalence of the TE/TM differential and Maxwell systems)**.** *Under invertibility of $\boldsymbol{\varepsilon}(z)$ and $\boldsymbol{\omega}$,* (14) *and* (16)*, together with the algebraic reconstruction in* (15)*, are equivalent to the source-free Floquet Maxwell system inside the isotropic slab for each nondegenerate transverse wavenumber.*

Proof. For TE, the s-component of the vector wave equation (6) gives (14), with its magnetic components recovered from Faraday's law. For TM, the κ-component of Ampère's law yields $\boldsymbol{h}' = \mathrm{i}\boldsymbol{\omega}\boldsymbol{\varepsilon}\boldsymbol{e}_\kappa$. The z-component gives $\boldsymbol{e}_z = -\kappa\boldsymbol{\varepsilon}^{-1}\boldsymbol{\omega}^{-1}\boldsymbol{h}$. Substitution into the s-component of Faraday's law gives the second equation in (15). Solving the first for $\boldsymbol{e}_\kappa = (1/\mathrm{i})\mathsf{A}\boldsymbol{h}'$ and differentiating yields (16). Every step is reversible under the stated invertibility assumptions. □

Write generically $\boldsymbol{u} = \boldsymbol{E}_s$ with $\mathsf{A} = \mathbf{I}$ for TE, and $\boldsymbol{u} = \boldsymbol{h}$ with $\mathsf{A} = \boldsymbol{\varepsilon}^{-1}\boldsymbol{\omega}^{-1}$ for TM. Define $\boldsymbol{p}_z = \mathsf{A}\boldsymbol{u}'$ and $\mathsf{Y} = \mathbf{I}$ (TE) or $\mathsf{Y} = \boldsymbol{\omega}^{-1}$ (TM). Exact outgoing vacuum conditions, expressed at $z = 0$ and $z = d$, are

$$\begin{aligned} \boldsymbol{p}_z(0) &= -\mathrm{i}\mathsf{Y}\boldsymbol{Q}\boldsymbol{u}(0), \\ \boldsymbol{p}_z(d) &= \mathrm{i}\mathsf{Y}\boldsymbol{Q}[\boldsymbol{u}(d) - 2\boldsymbol{u}^{\mathrm{inc}}(d)]. \end{aligned} \tag{17}$$

For a unit external current at $z_s > d$, the incident boundary traces in the carrier harmonic are

$$\begin{aligned} E^{\mathrm{inc}}_{s,0}(d) &= -\frac{\omega_0}{2q_0}\mathrm{e}^{\mathrm{i}q_0(z_s-d)}, \\ \big(H^{\mathrm{inc}}_{s,0}\big)_{(p_\kappa,p_z)} &= \frac{\mathrm{e}^{\mathrm{i}q_0(z_s-d)}}{2}\left(1, \frac{\kappa}{q_0}\right). \end{aligned} \tag{18}$$

All other incident harmonics vanish. At the upper interface the reflected TE electric trace is $\boldsymbol{u}(d) - \boldsymbol{u}^{\mathrm{inc}}(d)$ and the TM reflected magnetic trace is $\boldsymbol{h}(d) - \boldsymbol{h}^{\mathrm{inc}}(d)$. For the upward outgoing TM wave, $E^{\mathrm{sc}}_{\kappa,n} = (q_n/\omega_n)H^{\mathrm{sc}}_{s,n}$ and $E^{\mathrm{sc}}_{z,n} = -(\kappa/\omega_n)H^{\mathrm{sc}}_{s,n}$; this fixes all four TM dyadic entries from the two current inputs in (18).

The independent FDFD implementation divides the slab into N_z cells and solves the matrix finite-volume residual

$$\begin{aligned} \frac{\boldsymbol{p}_{j+1/2} - \boldsymbol{p}_{j-1/2}}{h} + \mathsf{V}_j\boldsymbol{u}_j &= 0, \\ \boldsymbol{p}_{j+1/2} &= \frac{\mathsf{A}_{j+1/2}}{h}(\boldsymbol{u}_{j+1} - \boldsymbol{u}_j). \end{aligned} \tag{19}$$

with $\mathsf{V}_j = \boldsymbol{\omega}^2\boldsymbol{\varepsilon}_j - \kappa^2\mathbf{I}$ (TE) or $\mathsf{V}_j = \boldsymbol{\omega} - \kappa^2\mathsf{A}_j$ (TM). The half-cell boundary values are eliminated using (17); in particular $\mathsf{B} = \mathbf{I} - (h/2)\mathsf{A}^{-1}\mathrm{i}\mathsf{Y}\boldsymbol{Q}$ at each surface gives

$$\begin{aligned} \boldsymbol{p}_{1/2} &= -\mathrm{i}\mathsf{Y}\boldsymbol{Q}\mathsf{B}^{-1}\boldsymbol{u}_0, \\ \boldsymbol{p}_{N_z+1/2} &= \mathrm{i}\mathsf{Y}\boldsymbol{Q}\mathsf{B}^{-1}(\boldsymbol{u}_{N_z-1} - 2\boldsymbol{u}^{\mathrm{inc}}). \end{aligned} \tag{20}$$

Thus the FDFD scheme solves differential Maxwell equations with surface admittances rather than reusing the Nyström vacuum volume kernel. The two solvers *share* the same finite Floquet material model and the outer Fourier–Bessel transform; their agreement is therefore a strong differential-versus-integral cross-check, but not independent three-dimensional Cartesian FDTD or a certificate of the spectral tail.

2.6 Source–receiver harmonic observable

The vector dyadic is not only a collection of reflection coefficients: for a specified source-current orientation $\boldsymbol{p}$ and linearly polarization-selective receiving field axis $\boldsymbol{u}$, it yields the complex harmonic observation

$$\begin{aligned} h_n(\rho; \boldsymbol{p}, \boldsymbol{u}) &= \boldsymbol{u}^T \mathsf{G}^{\mathrm{sc}}_{n0}(\rho; z_o, z_s)\boldsymbol{p}, \\ \mathcal{C}_{2/1} &= 20 \log_{10} |h_{+2}/h_{+1}| \,. \end{aligned} \tag{21}$$

Both vectors are real and unit normalized in the demonstration below; for complex receiving polarization a Hermitian projection convention must be specified instead. $\mathcal{C}_{2/1}$ measures a *scattered electric-field amplitude ratio*, not received port power, antenna realized gain, or S_{21}. The receiver projection retains interference between Cartesian components and makes the applicability of a scalar or first-Born surrogate directly testable. Since the slab is isotropic, TE and TM remain uncoupled polarization sectors even though temporal harmonics couple within each sector.

2.7 Energy identity and scope of the principal dyadic

The idealized instantaneous medium exchanges power with the modulation. For real $\varepsilon(z,t)$ and $\mu = 1$, the energy balance follows directly from Maxwell:

$$\frac{\partial}{\partial t}\frac{\varepsilon|\boldsymbol{E}|^2 + |\boldsymbol{H}|^2}{2} + \nabla \cdot (\boldsymbol{E} \times \boldsymbol{H}) = -\boldsymbol{E} \cdot \boldsymbol{J} - \frac{\partial_t \varepsilon}{2}|\boldsymbol{E}|^2. \tag{22}$$

The final term is the externally supplied modulation work. The separate signed-harmonic dipole tests below evaluate this term directly in the same idealized instantaneous constitutive model; they do not imply general pump stability. Light-line quadrature, harmonic truncation, depth resolution, and the κ tail require separate tests. High-contrast guided-mode peaks may require pole-aware complex-contour methods; unstable real-axis data from prior experiments are excluded.

3 Signed-Frequency and Dipole Observables

The principal volume-integral dyadic uses the positive-frequency sector $\omega_n > 0$. For separate real-signal tests we retain both signs of frequency, choose the outgoing branch with $\operatorname{Im} q_n \geq 0$ and $q_n/\omega_n > 0$ for propagating signed-frequency channels, and explicitly include the frequency-zero TM component. A source with $\omega_0 = 8 = 4\Omega$ is implemented with coherent $+\omega_0$ and $-\omega_0$ excitation in a symmetric signed Floquet basis; positive physical radiative frequencies are counted once.

In the TE sector, $\boldsymbol{E}_s'' + [\boldsymbol{\omega}^2\boldsymbol{\varepsilon}(z) - \kappa^2\mathbf{I}]\boldsymbol{E}_s = 0$ remains regular. In the TM sector the H_s representation in (16) is unsuitable at $\omega_n = 0$. Define $U_n = H_{s,n}/\omega_n$ by continuous extension and $V_n = \mathrm{i}E_{\kappa,n}$. For $\kappa > 0$, the following regular first-order system retains the static electric component:

$$\begin{aligned} &\boldsymbol{U}' = \boldsymbol{\varepsilon}(z)\boldsymbol{V}, \\ &\boldsymbol{V}' = [-\boldsymbol{\omega}^2 + \kappa^2\boldsymbol{\varepsilon}(z)^{-1}]\boldsymbol{U}, \\ &\boldsymbol{E}_\kappa = -\mathrm{i}\boldsymbol{V}, \quad \boldsymbol{E}_z = -\kappa\boldsymbol{\varepsilon}(z)^{-1}\boldsymbol{U}, \quad \boldsymbol{H}_s = \boldsymbol{\omega}\boldsymbol{U}. \end{aligned} \tag{23}$$

At $\omega_n = 0$ one may have $H_{s,n} = 0$ yet $E_{\kappa,n}, E_{z,n} \neq 0$; this harmonic carries no propagating power. The coincident $\kappa = \omega_n = 0$ limit requires an additional electrostatic condition and is not certified here. The signed open-channel action relation is $\sum_{\omega_n \neq 0} P_{\mathrm{out},n}/\omega_n = P_{\mathrm{in}}/\omega_0$ in the tested lossless plane-wave configuration, with the sign of ω_n retained. It is an established pseudounitary constraint [31], not a new reciprocity or conservation principle.

For a temporally even real scalar dielectric, the tested cross-frequency current-dyadic identity reads

$$\frac{\mathsf{G}^{EJ}_{nm}(\boldsymbol{\kappa}; z_r, z_s)}{\omega_n} = \left[\frac{\mathsf{G}^{EJ}_{mn}(-\boldsymbol{\kappa}; z_s, z_r)}{\omega_m}\right]^T, \tag{24}$$

where the transverse wavevector is reversed on source/receiver exchange. A simple unweighted transpose at fixed $\boldsymbol{\kappa}$ is generally not the correct diagnostic. Equation (24) is only claimed for the reciprocal scalar time-even drive, not for arbitrary traveling-wave modulation.

For a physical electric-dipole moment $\boldsymbol{p}_d$, $\boldsymbol{J} = -\mathrm{i}\omega_0 \boldsymbol{p}_d\, \delta(\boldsymbol{r} - \boldsymbol{r}_s)$ and the free-space reference is $P_0 = \omega_0^4 |\boldsymbol{p}_d|^2/(12\pi)$ in the normalized units. The propagating TE/TM angular spectra over both hemispheres determine

$$\begin{aligned} P_{\mathrm{rad}} &= \sum_{\omega_n > 0} \int_{4\pi} \frac{r^2}{2} \left(|E_{\theta,n}|^2 + |E_{\phi,n}|^2\right) \mathrm{d}\Omega_{\mathrm{s}}, \\ P_{\mathrm{src}} &= P_0 + \frac{\omega_0}{2} \operatorname{Im}[\boldsymbol{p}_d^* \cdot \boldsymbol{E}_{\mathrm{sc},0}(\boldsymbol{r}_s)], \\ P_{\mathrm{pump}} &= -\frac{1}{2} \int_{0<z<d} \left\langle \partial_t \varepsilon\, |\boldsymbol{E}_{\mathrm{real}}|^2 \right\rangle \mathrm{d}V. \end{aligned} \tag{25}$$

The last two quantities are evaluated independently: the source from the self-reaction Green field and the pump from the bulk field via transverse Parseval integration, *not* by subtracting radiated and source powers. Integrating (22) in the model predicts $P_{\mathrm{rad}} = P_{\mathrm{src}} + P_{\mathrm{pump}}$ in a stationary outgoing solution. These quantities are radiative power and imposed-source work, not antenna realized gain or port efficiency.

4 Numerical Results and Independent Checks

4.1 Experimental design, parameter separation, and static limit

The geometry and temporal/depth envelope in Fig. 1 fix the source and receiver conventions used throughout. All distances and frequencies in Table 1 use normalized $\varepsilon_0 = \mu_0 = c_0 = 1$ units; the illustrated dielectric is not a finite-area metasurface. The test sets below are deliberately distinct: the weakly driven convergence study uses $\alpha = 0.06$ and $N = 3$, the multi-method benchmark also uses $\alpha = 0.20$ and $N = 5$, the receiver test uses this moderate case, and the strong Born test uses $\alpha = 0.4$ and $\Omega/\omega_0 = 0.1$, and the dipole power study uses $\alpha = 0.3$ with separate positive and signed harmonic bases. Numerical discrepancies between these sets must not be pooled as one global error bound.

A static reference provides a material-level test independent of any temporal Floquet inversion. For $\alpha = 0$, uniform $\varepsilon_r = 1.4$ and $\kappa = 4.5$, let $q_0 = \sqrt{\omega_0^2 - \kappa^2}$, $q_1 = \sqrt{\varepsilon_r \omega_0^2 - \kappa^2}$, and

$$r_s = \frac{q_0 - q_1}{q_0 + q_1}, \quad r_p = \frac{q_1 - \varepsilon_r q_0}{q_1 + \varepsilon_r q_0}, \quad R_\nu = r_\nu \frac{1 - \mathrm{e}^{2\mathrm{i}q_1 d}}{1 - r_\nu^2 \mathrm{e}^{2\mathrm{i}q_1 d}}. \tag{26}$$

Independent axial FDFD solutions converge approximately quadratically to the analytic TE/TM response (Fig. 2). At $N_z = 256$, across the three tested κ values, the maximum relative TE/TM errors are 0.08633% and 0.06174%. This is a *static* Maxwell control, not a certificate for driven-harmonic reconstruction.

Table 1: Specified physical and numerical benchmark parameters. The primary dyadic and physical dipole studies use different stated harmonic bases.

Quantity	Value or convention
Layer and source	$d = 0.8$; $z_s = 1.22$ and $z_o = 1.17$ for dyadic receivers; vacuum exterior
Temporal law	$\omega_0 = 8$, $\Omega = 2$ except the stronger Born study; $\Delta\varepsilon_s = 0$, $\varepsilon = 1 + \alpha f(z)\cos\Omega t$
Main dyadic tests	$\alpha = 0.06$, $N = 3$ and $\alpha = 0.20$, $N = 5$; 201 offsets $\rho \in [0.02, 1.20]$; $\kappa_{\max} = 26$
Receiver/physical tests	$\alpha = 0.20$, $\Omega = 0.8$, $N = 5$ for receiver contrast; $\alpha = 0.3$; signed dipole $M = 9$
Verification axes	Independent axial Maxwell FDFD, continuous-depth transfer, analytical Fresnel, harmonic/angle/tail studies

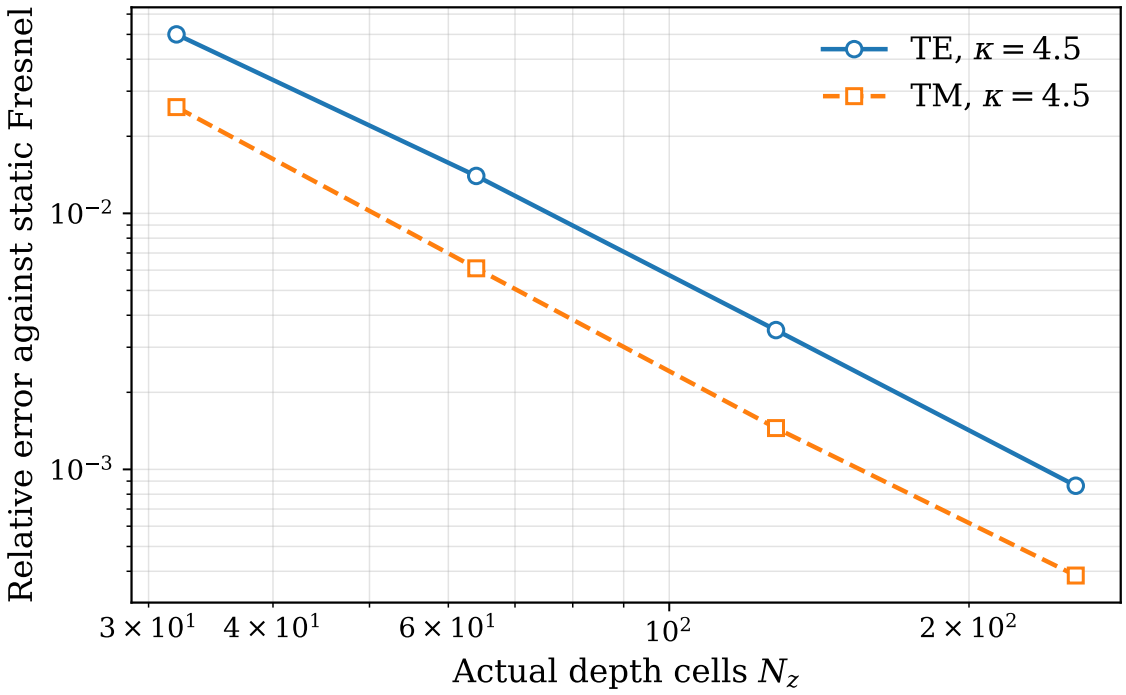


Figure 2: TE and TM independent axial Maxwell–FDFD refinement against the exact static uniform-slab Fresnel solution at $\kappa = 4.5$ and $\varepsilon_r = 1.4$; the reference is analytical, not a second numerical fit.

4.2 Independent differential versus integral solvers and revised convergence

For a fixed κ, the Nyström solver (9) and the independent axial Maxwell–FDFD scheme (19) discretize different governing integral and differential operators. The continuously profiled TE/TM Maxwell transfer solver additionally checks the axial cell approximation without a piecewise-constant depth profile. We report complex spectral block differences normalized by the reference Frobenius norm and full 201-receiver dyadic differences normalized by the same norm at each receiver. All physical-space comparisons that share the Fourier–Bessel nodes leave the radial quadrature as a *common* source of uncertainty.

An essential failure was detected in the old $N = 1$ three-harmonic calculation: two apparent real-axis features just above $\kappa = \omega_{+1} = 10$ occur at approximately 10.0000098271 (TM) and 10.0000154699 (TE). They are strongly altered when the omitted radiative $n = +2$ channel is retained. At their former locations the TM spectral norm changes from about 1218.54 ($N = 1$) to 0.16735 ($N = 2$); these near-threshold $N = 1$ spikes are not established poles of the fully coupled medium. The previously reported 0.2533% disagreement between FDFD and Nyström over 201

positions therefore characterizes their *shared* $N = 1$ *truncation*, not Floquet convergence. It is retained as a diagnostic legacy result rather than a main accuracy claim.

The repaired $N = 3$ reconstruction splits the κ integral at the retained channel light lines and separately refines the Floquet order N, quadrature order q, axial resolution and cutoff. Table 2 assembles the non-interchangeable tests; Fig. 3 shows independent axial FDFD refinement. The continuous-depth transfer and cell-based Nyström/Maxwell schemes are *not* called three independent full-Cartesian Maxwell simulations.

Table 2: Independent and incremental tests with their *actual denominators* and domains. The different rows are not a combined global error certificate.

Scoped test and error normalization	Maximum
Static FDFD versus analytic Fresnel TE/TM, $N_z = 256$	0.08633/0.06174%
Six κ points: FDFD versus continuous transfer, $N_z = 256$	0.3595%
201 receivers: $q = 96 \to 128$, continuous $N = 3$, Frobenius	1.80×10^{-5}%
201 receivers: $N = 2 \to 3$, continuous, $q = 96$	0.001352%
201 receivers: $\kappa_{\max} = 22 \to 26$, cell transfer	2.00×10^{-5}%
Signed dipole power: $M = 7 \to 9$, $\lvert\Delta P_{\mathrm{rad}}\rvert/P_0$	1.87×10^{-5}

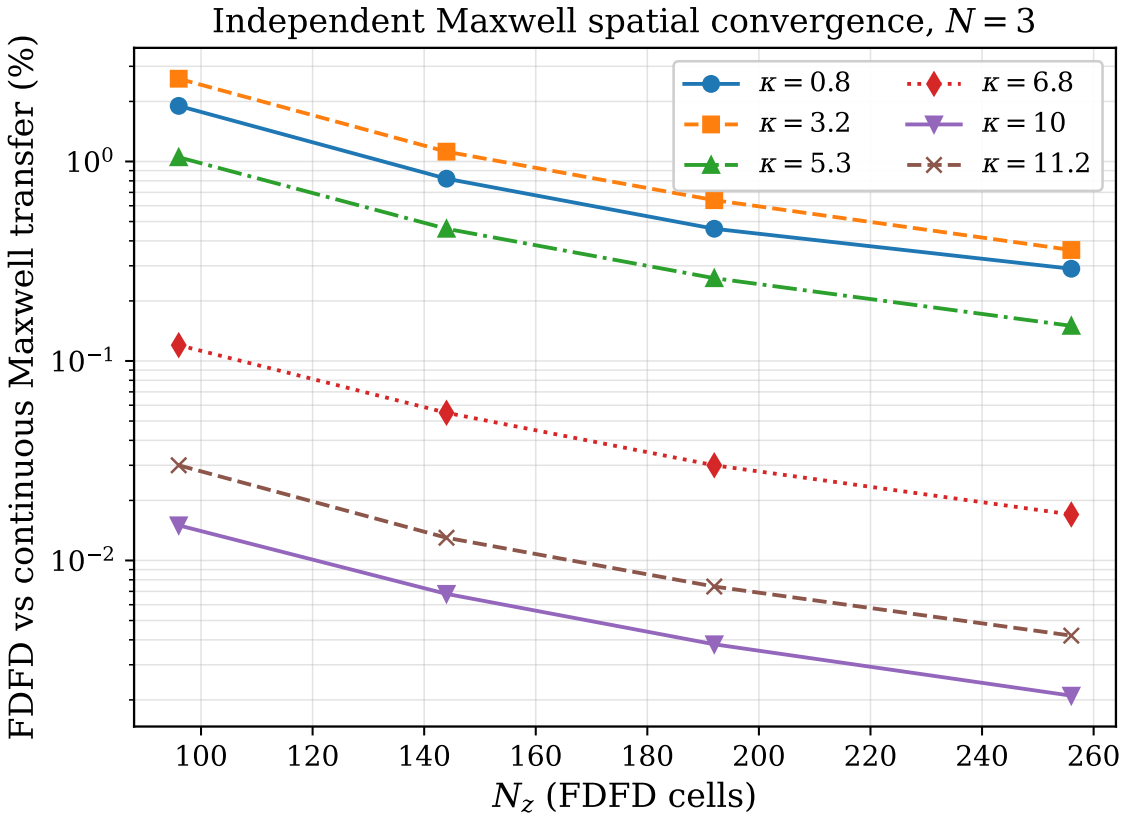


Figure 3: Selected nonstatic TE/TM spectral-channel comparisons of the independent axial Maxwell–FDFD discretization with the continuously profiled Maxwell transfer solution, including axial-grid refinement. These are fixed-transverse-wave-number checks, not an independent Cartesian three-dimensional simulation.

The repaired source–receiver response contains the five azimuthally allowed entries $G_{xx}, G_{yy}, G_{xz}, G_{zx}, G_{zz}$, not merely a scalar reflection channel. Figure 4 now emphasizes direct validation of that three-dimensional dyadic response in the moderate benchmark case: representative real and imaginary entries are shown together with the receiver-wise five-component discrepancy and the phase discrepancy of a nonzero component. These comparisons validate the

receiver-dependent five-component dyadic within the Floquet–Sommerfeld framework, not an independent Cartesian three-dimensional Maxwell solution.

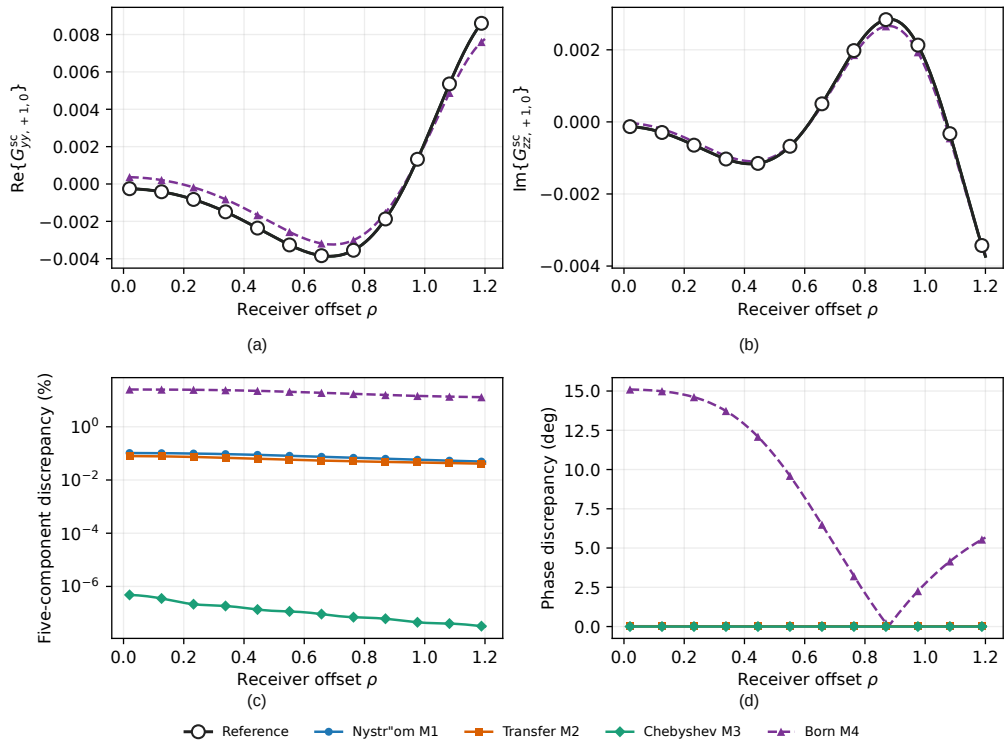


Figure 4: Independent validation of the corrected scattered electric-current dyadic for the moderate case ($\alpha = 0.20$, $\Omega = 0.8$, $N = 5$): (a) $\Re\{G^{\mathrm{sc}}_{yy,+1,0}\}$, (b) $\Im\{G^{\mathrm{sc}}_{zz,+1,0}\}$, (c) receiver-wise discrepancy aggregated over all five nonzero Cartesian entries, and (d) phase discrepancy of the nonzero $G_{yy,+1,0}$ component. The continuous-depth transfer reference employs refined Sommerfeld inversion; M1–M4 share the same Fourier–Bessel reconstruction. This is an independent solver cross-check within the common Floquet–Sommerfeld model, not a 201-point Cartesian 3-D Maxwell validation.

A matched-material-window test further checks the definition of the physical slab. Adding 0.20 and 0.15 units of vacuum on either side of the same layer and de-embedding the additional free-space propagation phase changes selected TE/TM spectral coefficients by at most 3.46×10^{-15} in normalized complex difference ($N = 2$, four κ samples). This is a useful domain-definition check, not thickness convergence of the dielectric or a finite lateral-size experiment.

4.3 Four-method full-dyadic accuracy, cost, and reuse

Having separated harmonic, depth, and Sommerfeld discretization errors, we compare the present Floquet volume-integral Nyström method (M1) with sliced Maxwell–Floquet transfer (M2), an independently coded Chebyshev-collocation Maxwell Green boundary-value solver (M3), and first Born (M4). M3 is *not* a reproduction of the distinct two-dimensional half-space formulation in [15]. The common model, point-current normalization, 201 receiver offsets, five independent complex entries, and $n = -2, \ldots, +2$ outputs are identical. All methods share the Fourier–Bessel inversion; the reference is continuously profiled Maxwell transfer with refined radial quadrature, not an independent 3-D Cartesian Maxwell simulation.

The two accuracy-certified settings are a weak regime ($\alpha = 0.06$, $\Omega/\omega_0 = 0.25$, $N = 3$) and a moderate regime ($\alpha = 0.20$, $\Omega/\omega_0 = 0.10$, $N = 5$). The global metric is the complex RMS error aggregated over *all five harmonics, five dyadic entries, and 201 receivers*, rather than a selected near-zero channel. At a common acceptance threshold of 0.1%, all three nonperturbative methods

pass with the settings in Table 3, while M4 fails. Figure 5 demonstrates their complex point-source fields and receiver-wise discrepancy in the moderate case. The transfer and Chebyshev solvers actually yield smaller errors than Nyström at the tested resolutions; the comparison supports *accurate formulation and nonperturbative necessity*, not intrinsic Nyström accuracy superiority.

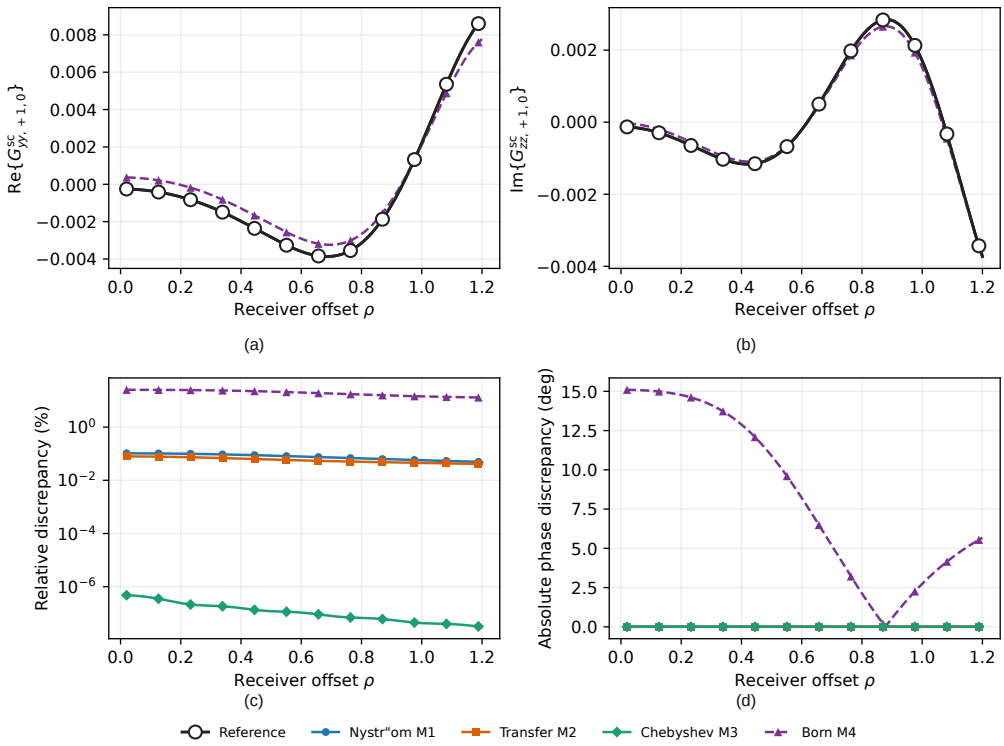


Figure 5: Four-method comparison for $\alpha = 0.20$, $\Omega = 0.8$, $N = 5$ and 201 receiver offsets: selected complex entries, receiver-wise five-component discrepancy, and phase difference where the reference is not near zero. The continuous-depth transfer reference employs refined Sommerfeld integration; M1–M4 share the Fourier–Bessel transform. A 1% reference-amplitude floor is used only for the displayed near-null discrepancy.

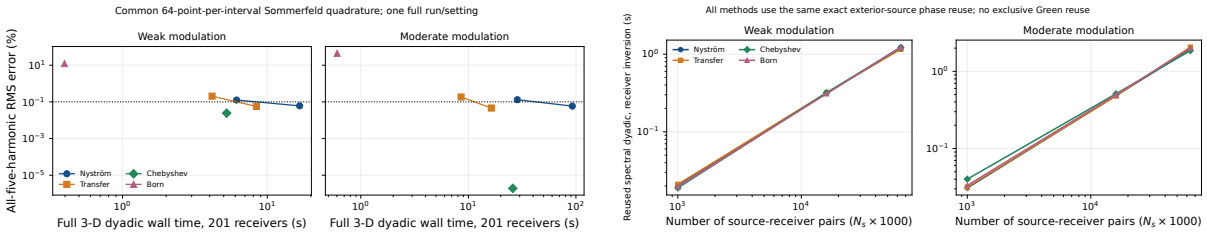
Table 3: Matched-threshold ($< 0.1\%$) full-3-D complex-dyadic accuracy and measured end-to-end cost (five harmonics, five independent entries, 201 receivers). Times include axial spectral solves and common Sommerfeld reconstruction, using one BLAS thread and one complete 3-D timed run per configuration; peak process RSS includes Python overhead. Errors compare with the refined continuous-depth reference. M4 does not pass the target. Settings are a common *error threshold*, not identical achieved errors or proven globally optimal configurations.

Regime	Method (depth setting)	Global error (%)	Total time (s)	Peak RSS (MiB)	Meets 0.1%?
Weak	M1 Nyström ($N_z = 48$)	0.06068	16.72	172.5	Yes
	M2 sliced transfer (96)	0.05654	8.40	154.9	Yes
	M3 Chebyshev ($P = 20$)	0.02436	5.24	156.0	Yes
	M4 first Born	12.3739	0.40	154.4	No
Moderate	M1 Nyström ($N_z = 48$)	0.05899	92.48	214.8	Yes
	M2 sliced transfer (96)	0.04621	16.34	158.6	Yes
	M3 Chebyshev ($P = 24$)	1.93×10^{-6}	25.87	167.9	Yes
	M4 first Born	44.7646	0.60	158.1	No

Figures 6(a) and (b) give the measured end-to-end accuracy–cost evidence. For the *representative settings retained in Table 3*, sliced transfer is about 1.99× (5.66×) faster and Chebyshev

about 3.19× (3.58×) faster than M1 in the weak (moderate) configuration. The additional Chebyshev sweep in Fig. 6(a),(b) also reaches the 0.1% target at $P = 14$, with observed times of 2.46 s and 9.42 s, respectively; these are separate single-run measurements and are not substituted silently into the earlier table. First Born has *one measured resolution per regime*, hence one point in each accuracy–cost panel, not a convergence curve. Its omitted higher-order harmonic interactions constitute a model-order limitation: numerical quadrature refinement cannot recover those missing interactions, although convergence of Born discretization itself was not exhaustively tested. The table does not establish a *universal* ranking: end-to-end runs were timed once per selected configuration, and no equal-accuracy optimal-tuning frontier or all-hardware claim was established. The stronger $\alpha = 0.4$, $N = 3$ test is excluded from positive benchmarking because a narrow $\kappa \simeq 10.552$ feature fails harmonic and radial convergence.

For fixed spectral data, source-height and observation-height changes can be factored by outgoing channel phases $\exp[\mathrm{i}q_0\Delta z_s + \mathrm{i}q_n\Delta z_o]$. Direct recomputation versus this spectral reuse agrees to 3.47×10^{-12} or better among M1–M3. Figures 6(c) and (d) record 1, 16, and 64 source queries and 201/1000 receiver offsets: the 64×1000 reconstruction stage takes approximately 1.16–1.23 s in the weak regime and 1.86–2.06 s in the moderate regime. *All four* implementations exploit the same reconstruction reuse; the value of the dyadic interface is therefore practical, not a demonstrated exclusive computational advantage of Nyström.



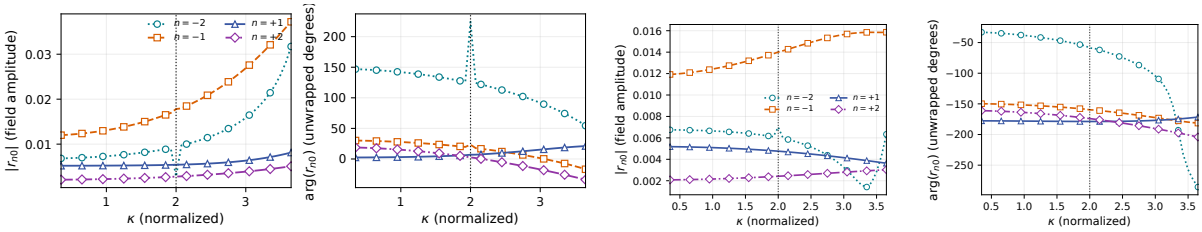
(a) (b) (c) (d)

Figure 6: Four-method accuracy and computational-cost comparison. (a),(b) End-to-end three-dimensional five-harmonic dyadic error versus execution time for weak and moderate modulation, respectively, with a multi-order Chebyshev sweep and the previously recorded Nyström, transfer, and first-Born settings. Born has only one timed numerical setting per regime and does not meet the 0.1% accuracy threshold; its plotted point is not a numerical-convergence curve. (c),(d) Cached-spectral source–receiver reconstruction cost for weak and moderate modulation, respectively, shared by all four methods. Single-run timings are hardware- and setup-specific; phase reuse is not exclusive to M1.

4.4 Complex sidebands and the nonperturbative requirement

Having quantified full-dyadic accuracy and end-to-end cost across four workflows, we turn to the physical consequences of frequency mixing in the model itself. Figure 7 shows both *magnitude and unwrapped phase* of plane-wave complex reflection amplitudes r_{n0} for TE and TM, $n = \pm 1, \pm 2$, using $\alpha = 0.3$, $N = 3$, $d = 0.8$, and $0.35 \le \kappa \le 3.65$. TE amplitudes refer to electric, TM to magnetic modal fields. Their values cannot be interpreted as powers or as elements of the complete reconstructed point-source dyadic. Near $\kappa = 2$, the $n = -3$ channel reaches its propagation threshold. Separate refined signed-frequency and differential Maxwell checks resolve a narrow TE feature, whereas the precise TM value at the cutoff is truncation-sensitive; the present 45-point overview must not be interpreted as a pole or resonance identification. Signed-frequency spot comparisons for four sidebands gave maximum relative differences 1.80×10^{-10} (TE) and 2.36×10^{-5} (TM), in the sampled angular channels; no global frequency-sign convergence follows.

The finite-matrix inverse (11) permits repeated sideband transitions. An independently



(a) (b) (c) (d)

Figure 7: Plane-wave complex spectral reflection r_{n0} for four sidebands ($n = -2, -1, +1, +2$): (a) TE magnitude, (b) TE unwrapped phase, (c) TM magnitude, and (d) TM unwrapped phase, for $\alpha = 0.3$, $N = 3$, $\omega_0 = 8$, and $\Omega = 2$. Symbols mark selected samples from the 45-point transverse-wave-number grid and the vertical dotted line marks the $\kappa = 2$ cutoff of the $n = -3$ channel. The narrow cutoff feature is not resolved by this coarse overview and is not identified as a physical pole. These are modal field amplitudes, not power efficiencies or point-current dyadic entries.

integrated *first Born* $+1$ block for the single-tone perturbation is

$$\mathsf{G}^{\mathrm{B1}}_{+1,0} = \frac{\mathrm{i}\omega_0\alpha\omega_{+1}^2}{2}\int_0^d f(z)\mathsf{G}^{(0)}_{+1}(z_o, z)\mathsf{G}^{(0)}_{0}(z, z_s)\mathrm{d}z, \tag{27}$$

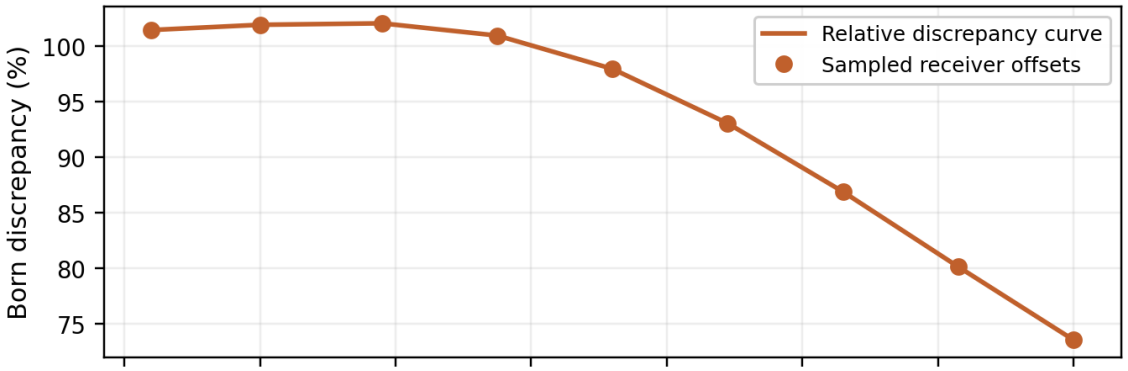
with the same current normalization. In a stronger $\alpha = 0.4$, $\kappa = 6.8$ test and $N = 8$, the spectral Frobenius discrepancy of the full block relative to Born is 111.18% at $\Omega/\omega_0 = 0.05$ and 135.21% at 0.10. The $+2$ response vanishes at first order for a single temporal tone but is nonzero in the complete finite system. The same breakdown persists after Fourier–Bessel inversion: for the $\Omega/\omega_0 = 0.10$, $N = 5$, $N_z = 48$, $\kappa_{\max} = 26$ test, the full five-entry three-dimensional response differs from first Born by 73.57–102.38% at 201 receiver offsets $0.12 \le \rho \le 0.80$ (Fig. 8). Independent axial FDFD and Nyström using the *same* finite-harmonic inversion differ by 0.359–0.923% over these receiver positions. This is quantitative evidence for *when* multiple Floquet scattering matters, not an assertion that Floquet inversion itself is new or that every strong-pump solution is stable.

4.5 Receiver-conditioned higher-harmonic selection

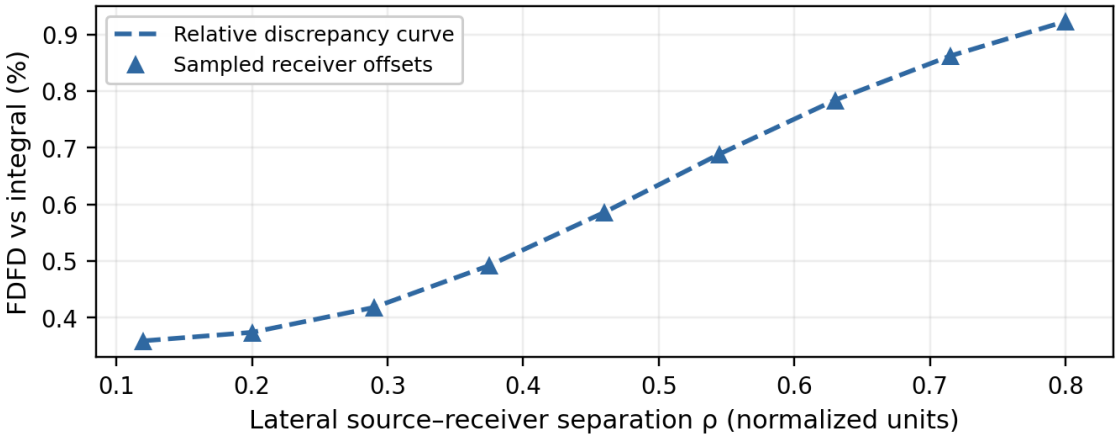
The full dyadic also makes an electromagnetic *source–receiver* observation possible that is not determined by a plane-wave sideband coefficient alone. We now use the same moderate setting as the accuracy benchmark ($\alpha = 0.20$, $\Omega = 0.8$, $N = 5$, $z_s = 1.22$, $z_o = 1.17$). For real linear orientations $\boldsymbol{p} = (\cos 18°, 0, \sin 18°)^T$ and $\boldsymbol{u} = (\cos 60°, 0, \sin 60°)^T$, Eq. (21) combines the xx, xz, zx, and zz Green components, including their complex phases. At $\rho = 0.3091$ ($\simeq 0.394\lambda_0$), the continuous-depth reference gives $|h_{+1}| = 1.09646 \times 10^{-5}$ and $|h_{+2}| = 2.67390 \times 10^{-4}$, hence $\mathcal{C}_{2/1} = +27.743$ dB. At $\rho = 0.7044$ ($\simeq 0.897\lambda_0$), the same source and receiver orientations instead give -30.436 dB: a 58.18-dB spatial reversal of the *scattered-field amplitude contrast* (Fig. 9).

The mechanism is destructive *vector interference* within h_{+1}, not TE-to-TM conversion: the complex contributions from G_{xx}, G_{xz}, G_{zx}, and G_{zz} nearly cancel, while h_{+2} remains finite (Fig. 10). M1, M2, and M3 predict $+27.979$, $+28.001$, and $+27.743$ dB at the first receiver, respectively; first Born gives $h_{+2} = 0$ for single-tone modulation. Control orientations $x \to x$ and $y \to y$ yield contrasts -7.138 and -9.768 dB at the same ρ, which directly exposes the role of orientation-dependent projection. Although the global dyadic is accurate to better than 0.1%, relative errors of the *near-cancelled* h_{+1} are 2.79% (M1) and 3.65% (M2); we do not transfer global accuracy bounds indiscriminately to a near-null observable.

The selected contrast is *tuned*, not universally robust: among sampled changes of both angles by $\pm 1°$ and ρ by ± 0.0059, its minimum remains $+10.93$ dB, whereas $\pm 2°$ and ± 0.0118 give a minimum $+4.09$ dB and larger offsets may reverse it. Varying α to 0.16 and 0.24 yields



(a)



(b)

Figure 8: Strong-modulation +1 scattered point-current dyadic versus lateral source–receiver separation: (a) first-Born versus finite nonperturbative five-entry Frobenius discrepancy, shown as a relative-discrepancy curve with sampled receiver offsets; (b) independent axial Maxwell–FDFD versus Nyström discrepancy, again shown as a relative-discrepancy curve with sampled receiver offsets. The 201 receiver offsets, $\alpha = 0.4$, $N = 5$, and $\Omega/\omega_0 = 0.10$ are distinct from the weak-modulation convergence example.

+9.34 and +11.50 dB, respectively, with controlled Chebyshev results. The receiver projection is a field observable, not a calibrated S_{21} or port power; it illustrates a predictive *use* of the three-dimensional vector dyadic, not a claim of first-ever polarization/frequency selectivity or an Nyström-only phenomenon [20–22, 26].

4.6 Signed harmonics, radiative observables, and source–pump balance

The receiver-projected fields of Section 4.5 are distinct from radiated power: to make that distinction explicit, the conversion plots of Fig. 7 are next connected to an actual electric dipole. The signed-frequency Maxwell model uses coherent ± 8 source harmonics, retains the zero-frequency TM electrostatic field, and evaluates both upper and lower radiative hemispheres. Its TM zero-mode E_z at the slab center is nonzero for $\kappa = 1.3$, $\alpha = 0.3$, and the independent $N_z = 1024$ FDFD agrees with the continuous solution to 1.07×10^{-5} relative amplitude in the tested $N = 5$ case. For a noncommensurate signed test ($\omega_s = 1.3$, $\Omega = 2$, $N = 5$), TE/TM pump power balances and signed wave-action relations have $\mathcal{O}(10^{-12})$ or smaller residuals; no new conservation law is claimed. Twelve source-exchange cases for the 3×3 complex spectral electric-current dyadic satisfy the frequency-weighted identity (24) with maximum relative residual

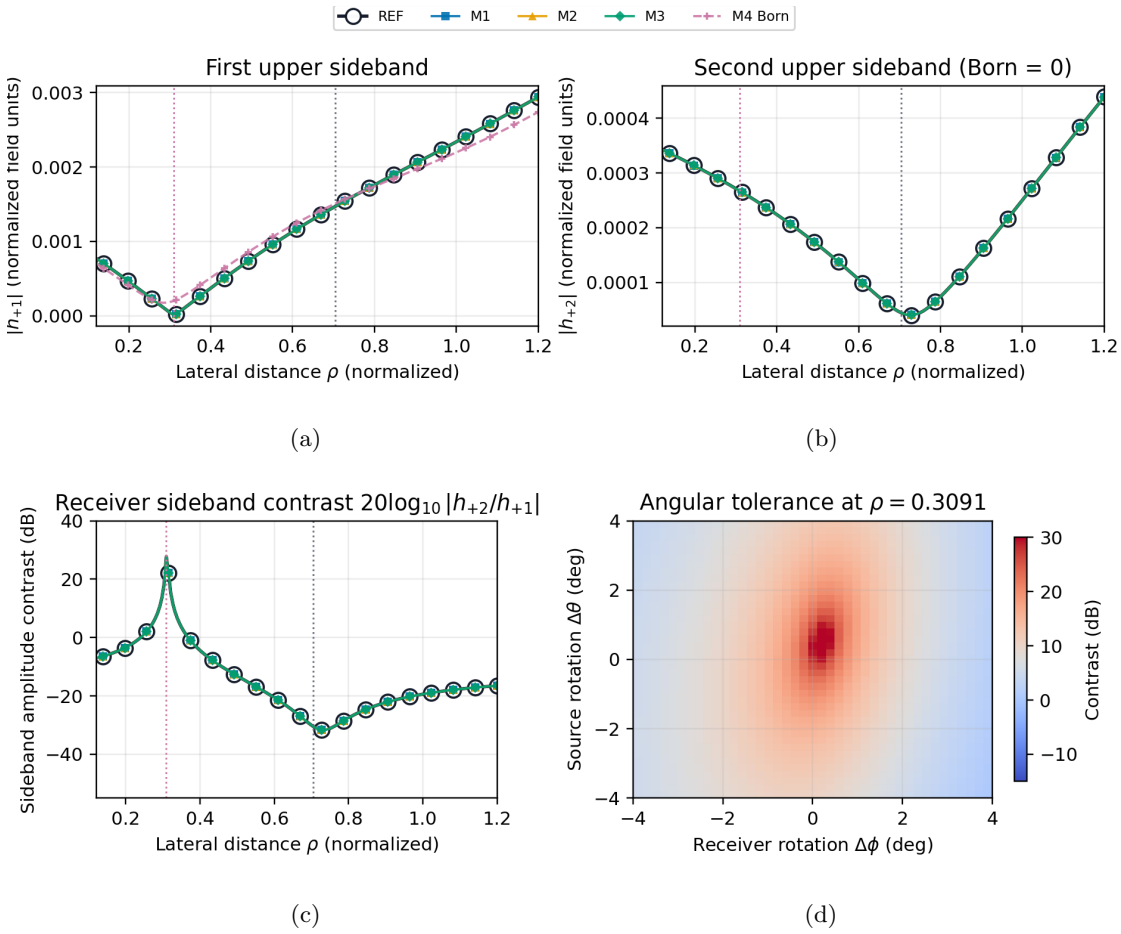


Figure 9: Receiver-conditioned scattered-field harmonic selectivity for $\alpha = 0.20$, $\Omega/\omega_0 = 0.10$, $N = 5$, and fixed source/receiver orientations $(18°, 60°)$: (a) $|h_{+1}|$, (b) $|h_{+2}|$, (c) $20\log_{10}|h_{+2}/h_{+1}|$ versus lateral separation, and (d) sampled angular tolerance near $\rho = 0.3091$. M1–M3 agree with continuous-depth transfer while first-order Born predicts a zero +2 term. The enhanced contrast is localized and orientation-dependent, not a universal gain enhancement.

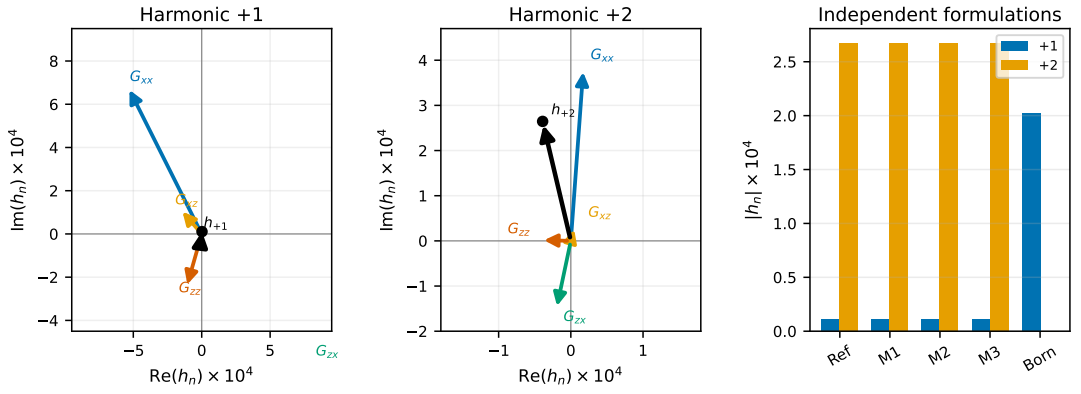


Figure 10: Complex-vector explanation and solver control at $\rho = 0.3091$. (a) The weighted xx, xz, zx, zz contributions to h_{+1} nearly cancel; (b) the contributions to h_{+2} do not; (c) reference, Nyström, transfer, Chebyshev, and first-Born field amplitudes. The vectors are components of a receiver *projection* of the electric-current dyadic, not separate TE/TM polarization-conversion pathways.

2.25×10^{-10}.

Figure 11 connects the signed-frequency Maxwell dipole solution to both *angle-resolved radiation* and *hemispherically integrated power*. Define the radiated intensity $U_n(\theta, \phi) = \mathrm{d}P_n/\mathrm{d}\Omega_{\mathrm{solid}}$, so that $P_{n,\mathrm{up/down}} = \int_{\mathcal{H}_{\mathrm{up/down}}} U_n(\theta, \phi)\, \mathrm{d}\Omega_{\mathrm{solid}}$. Panels (a) and (b) display the dimensionless *far-field meridional cuts* $4\pi U_n/P_0$ on a logarithmic radial scale for the horizontal (p_y, azimuth $\phi = 45°$) and vertical (p_z, azimuth $\phi = 0°$) dipoles, respectively. The upper and lower halves of each polar panel correspond to the outgoing $+z$ and $-z$ directions, respectively. These single-azimuth cuts show angular structure, but *cannot alone determine integrated radiated power*. Panels (c) and (d) report the corresponding powers integrated over *all azimuths* and over the entire upper or lower hemisphere for each sideband. All panels omit the carrier $n = 0$ in order to resolve the converted orders $n = \pm 1, \pm 2$; the normalization P_0 is the free-space dipole power at ω_0. Neither the polar-cut radius nor the integrated radiated power is antenna realized gain, directivity, or a measured port response.

The coherent real-dipole signed-chain $M = 9$ result gives the *total power including the carrier*, $P_{\mathrm{rad}}/P_0 = 1.0223360$ for p_y and 1.0315995 for p_z, in the representative $\alpha = 0.3$ configuration. At a common angular quadrature, the $M = 7 \to 9$ total-power changes are $1.8688 \times 10^{-5} P_0$ and $1.6477 \times 10^{-5} P_0$, respectively. Reintegrating the same Maxwell–Floquet angular amplitudes reproduces the $M = 9$ hemispheric powers to numerical roundoff; a change to $\mu = \cos\theta$ with independent angular quadrature nodes yields at most 0.062% relative discrepancy in the tested cases. This checks angular integration within the same Maxwell model, *not* an independent full-Cartesian 3-D Maxwell solution. The signed extra channels have a small effect *in this regime*, but this does not follow for arbitrary parametric resonances.

In the $N = 3$ *positive-frequency* reference calculation, separate far-field integration, point-source reaction, and bulk pump-work evaluation give the quantitative budget in Table 4. The directly computed power-balance residuals are $2.11 \times 10^{-8} P_0$ and $2.44 \times 10^{-8} P_0$, respectively. These *intra-model balance residuals* are not global numerical errors: the more complete signed-chain power changes at the $10^{-5} P_0$ level under harmonic refinement, as listed in Table 2. A small excess of radiated over free-space power is therefore attributable to pump work within the tested lossless model, not realized antenna gain or guaranteed signal improvement.

Table 4: Independently evaluated horizontal and vertical dipole power budget, normalized by the corresponding P_0, $\alpha = 0.3$ and positive-frequency $N = 3$ model.

Quantity	p_y	p_z
P_{rad}/P_0	1.0223173144	1.0315830466
P_{src}/P_0	0.9992404107	0.9997565154
P_{pump}/P_0	0.0230769248	0.0318265556
$\lvert P_{\mathrm{rad}} - P_{\mathrm{src}} - P_{\mathrm{pump}}\rvert/P_0$	2.11×10^{-8}	2.44×10^{-8}

The meridional angular field observables in Fig. 11(a)–(b) remain distinct from the receiver-projected scattered-field contrast in Fig. 9, the integrated powers in Fig. 11(c)–(d), and antenna realized gain.

4.7 Scope of the claims and outstanding validation gates

The tests support three distinct statements. First, the Nyström point-current dyadic is consistent with analytic limits, differential axial Maxwell equations, and independent Maxwell transfer/Green-BVP implementations within specified harmonic and quadrature truncations. Second, full multiple-scattering calculations are necessary in the examined moderate and strong regimes: first Born cannot recover the +2 sideband of a single-tone modulation and gives large full-dyadic discrepancies. Third, complex vector interference can produce a localized, receiver-conditioned reversal of sideband selectivity; its prediction requires retaining source/receiver orientations and the complex cross entries. This third *physical application* is the strongest result

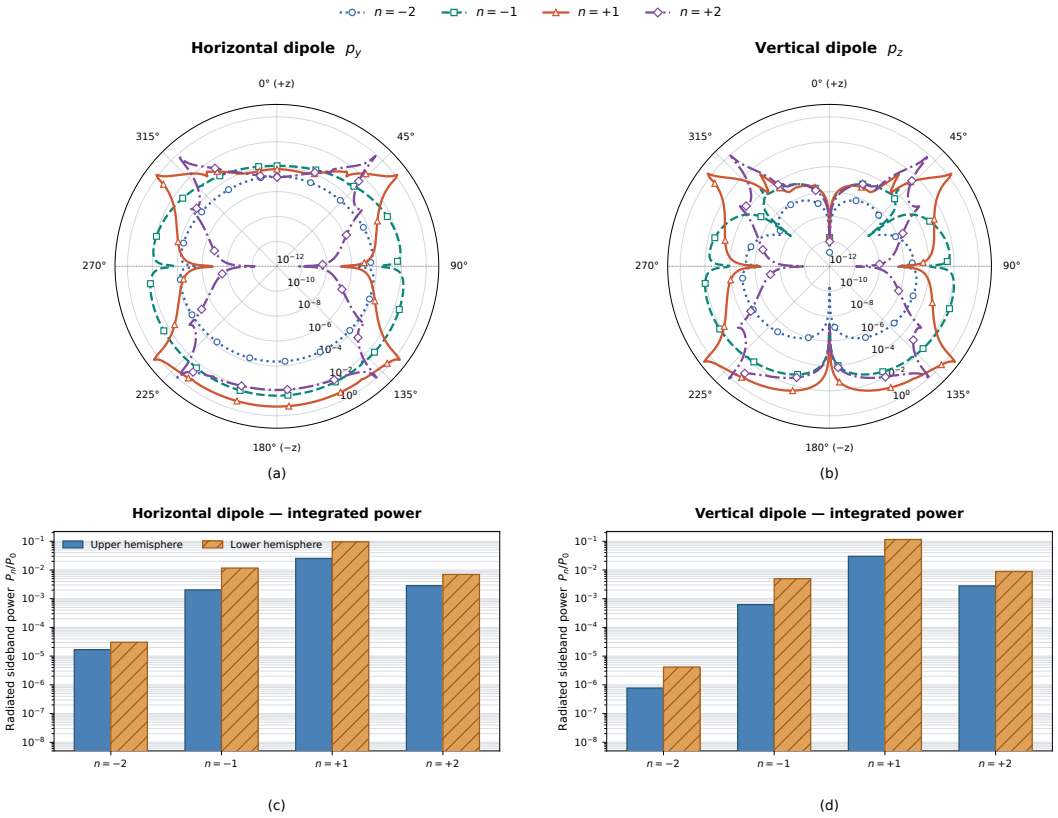


Figure 11: Physical point-electric-dipole radiation above the periodically modulated dielectric ($\alpha = 0.3$, $\omega_0 = 8$, $\Omega = 2$, signed-frequency $M = 9$). (a) Horizontal y-oriented and (b) vertical z-oriented dipole: logarithmic-radius meridional cuts of normalized radiated intensity $4\pi U_n(\theta, \phi)/P_0$, with $\phi = 45°$ and $\phi = 0°$, respectively. The upper/lower semicircles correspond to $+z/-z$ radiation; these cuts are not full-solid-angle distributions. (c) Horizontal and (d) vertical dipole: the corresponding upper- and lower-hemisphere P_n/P_0, integrated over all azimuths with 24 Gauss points per original spectral interval. All panels display only $n = \pm 1, \pm 2$; $n = 0$ is omitted for legibility. The polar intensity and hemispheric powers are *not* antenna gain, directivity, accepted port power, or realized gain.

of the unified characterization, but it is not a proof that a competing Floquet–Sommerfeld formulation cannot reproduce it.

The matched-threshold benchmark in Table 3 directly rules out a generic speed, memory, or accuracy advantage of the present Nyström implementation over M2/M3. Likewise, spectral source/receiver reuse is shared by all four methods. The relevant prior studies of Green functions [15], generalized Floquet scattering/pseudounitarity [27, 31], near-/far-field dipole control [26], and polarization/frequency conversion [20–22] make any unrestricted novelty-priority claim untenable on the present evidence. The added value is a reproducible, full-vector *electric-current source-to-receiver workflow* with cross-validated, receiver-specific physical predictions, not a new fundamental theorem.

Finally, a finite-time one-dimensional Yee test showed no obvious exponential growth up to normalized $t = 110$ for the selected finite-depth slab, but this is not a global pump-stability certificate. A distinct infinite uniform Hill-equation example is unstable and must not be conflated with the finite open slab. Outgoing complex-pole/pump stability over all κ, fully independent Cartesian 3-D Maxwell validation, and a dispersive physically pumpable material model remain open. The results are also restricted to a laterally infinite dielectric, not a finite-aperture metasurface or a measured antenna port.

5 Conclusion

The scattered electric-current dyadic of a three-dimensional point source above a laterally infinite, finite-thickness dielectric slab with instantaneous periodic modulation has been reconstructed using nonperturbative Floquet–Nyström spectral equations with the TE/TM channels, longitudinal contact term, and outgoing Fourier–Bessel transform. Fresnel benchmarks, independent axial Maxwell FDFD, continuously profiled Maxwell transfer, and a separately coded Chebyshev Green-BVP solver establish explicitly bounded agreement for the five complex Cartesian entries. A four-method, five-harmonic 201-receiver benchmark finds that Nyström meets a 0.1% full-dyadic error threshold in two regimes, but sliced transfer and Chebyshev are faster and use less peak memory at the tested settings; first Born fails the accuracy threshold. Multi-query Green-spectrum reuse is useful but shared by all four approaches.

The central physical example projects the verified complex dyadic onto a rotated source and linearly selective receiver. An interference-driven second-to-first sideband contrast of +27.74 dB at $\rho = 0.3091$ reverses to −30.44 dB at $\rho = 0.7044$, with independent nonperturbative agreement and quantified angular/parameter sensitivity. This result explains why retaining complex vector and cross-component information matters for a receiver-conditioned frequency-conversion observable. Signed-frequency and zero-frequency TM calculations separately connect the mathematical model to physical-dipole polar far-field cuts, azimuth-integrated harmonic radiated powers, and independently evaluated pump/source work. Polar radiation-intensity cuts are not antenna gain or directivity, and their angular-integration consistency is not an independent 3-D full-wave certificate. No exclusive Nyström superiority, global pump stability, dispersive-material realizability, or independent full Cartesian 3-D Maxwell validation is claimed. The paper's bounded contribution is a reproducible full-vector source–receiver characterization and its quantitatively validated harmonic-selective application.

Data Availability

The datasets used and/or analysed during the current study are available from the corresponding author on reasonable request.

References

[1] E. Galiffi, R. Tirole, S. Yin, H. Li, S. Vezzoli, P. A. Huidobro, M. G. Silveirinha, R. Sapienza, A. Alù, and J. B. Pendry, "Photonics of time-varying media," *Advanced Photonics*, vol. 4, no. 1, Art. no. 014002, 2022, doi: 10.1117/1.AP.4.1.014002.

[2] G. Ptitcyn, M. S. Mirmoosa, A. Sotoodehfar, and S. A. Tretyakov, "A tutorial on the basics of time-varying electromagnetic systems and circuits: Historic overview and basic concepts of time-modulation, *IEEE Antennas Propag. Mag.*, vol. 65, no. 4, pp. 10–20, 2023, doi: 10.1109/MAP.2023.3261601.

[3] A. M. Shaltout, V. M. Shalaev, and M. L. Brongersma, "Spatiotemporal light control with active metasurfaces, *Science*, vol. 364, no. 6441, Art. no. eaat3100, 2019, doi: 10.1126/science.aat3100.

[4] S. B. Ịplikçioğlu and M. I. Aksun, "Analytical modeling of time-varying and dispersive metasurfaces with surface susceptibility operators," *Phys. Rev. B*, vol. 111, Art. no. 245141, 2025, doi: 10.1103/lcs1-9llz.

[5] E. Lustig, Y. Sharabi, and M. Segev, "Topological aspects of photonic time crystals, *Optica*, vol. 5, no. 11, pp. 1390–1395, 2018, doi: 10.1364/OPTICA.5.001390.

[6] X. Wang, P. Garg, M. S. Mirmoosa, A. G. Lamprianidis, C. Rockstuhl, and V. S. Asadchy, "Expanding momentum bandgaps in photonic time crystals through resonances, *Nature Photonics*, vol. 19, pp. 149–155, 2025, doi: 10.1038/s41566-024-01563-3.

[7] H. Moussa, G. Xu, S. Yin, E. Galiffi, Y. Radi, and A. Alù, "Observation of temporal reflection and broadband frequency translation at photonic time interfaces, *Nature Physics*, vol. 19, pp. 863–868, 2023, doi: 10.1038/s41567-023-01975-y.

[8] Y. Hadad, D. L. Sounas, and A. Alù, "Space–time gradient metasurfaces, *Phys. Rev. B*, vol. 92, Art. no. 100304(R), 2015, doi: 10.1103/PhysRevB.92.100304.

[9] S. Taravati, N. Chamanara, and C. Caloz, "Nonreciprocal electromagnetic scattering from a periodically space–time modulated slab and application to a quasisonic isolator, *Phys. Rev. B*, vol. 96, Art. no. 165144, 2017, doi: 10.1103/PhysRevB.96.165144.

[10] M. Salehi, M. Memarian, and K. Mehrany, "Time-varying equivalent circuit for dynamically modulated dielectric slabs and its implications for stability analysis, *Opt. Express*, vol. 32, no. 14, pp. 24899–24925, 2024, doi: 10.1364/OE.523273.

[11] Y. Sun, S. Fan, and G. Hu, "Formulation of dispersive and dissipative time-varying media as a Floquet matrix eigenproblem, *Phys. Rev. Lett.*, vol. 135, Art. no. 156903, 2025, doi: 10.1103/lcmw-qrrp.

[12] W. Zhang, B. Wang, and W. Cai, "A matrix basis formulation for the dyadic Green's functions of Maxwell's equations in layered media," *SIAM J. Appl. Math.*, vol. 82, no. 5, pp. 1710–1732, 2022, doi: 10.1137/21M1429102.

[13] A. Arlouski, L. Gao, D. Gao, and A. Novitsky, "General and concise operator approach to the dyadic Green's function of layered media," *Phys. Rev. A*, vol. 114, Art. no. 033517, 2026, doi: 10.1103/5x4z-q37v.

[14] M. Kreiczer and Y. Hadad, "Green's function theory of spatiotemporally modulated loaded wire surface," *Phys. Rev. Research*, vol. 5, Art. no. 043256, 2023, doi: 10.1103/PhysRevResearch.5.043256.

[15] M. Kreiczer, B. Z. Steinberg, and Y. Hadad, "Localized source above a time-modulated dielectric half-space: Green's function theory," *Phys. Rev. Research*, vol. 6, Art. no. 013277, 2024, doi: 10.1103/PhysRevResearch.6.013277.

[16] K. Wapenaar and E. Slob, "Green's matrix and propagator matrix for three-dimensional electromagnetic wave propagation and scattering in a time-variant material," *Progress In Electromagnetics Research*, vol. 186, pp. 11–23, 2026, doi: 10.2528/PIER26043001.

[17] L. Zhang *et al.*, "Space-time-coding digital metasurfaces, *Nature Commun.*, vol. 9, Art. no. 4334, 2018, doi: 10.1038/s41467-018-06802-0.

[18] K. Lee, J. Son, J. Park, B. Kang, W. Jeon, F. Rotermund, and B. Min, "Linear frequency conversion via sudden merging of meta-atoms in time-variant metasurfaces, *Nature Photonics*, vol. 12, pp. 765–773, 2018, doi: 10.1038/s41566-018-0259-4.

[19] X. Guo, Y. Ding, Y. Duan, and X. Ni, "Nonreciprocal metasurface with space–time phase modulation, *Light Sci. Appl.*, vol. 8, Art. no. 123, 2019, doi: 10.1038/s41377-019-0225-z.

[20] J. Yang, J. C. Ke, W. K. Cao, M. Z. Chen, Q. Cheng, V. Galdi, and T. J. Cui, "Simultaneous conversion of polarization and frequency via time-division-multiplexing metasurfaces," *Adv. Opt. Mater.*, vol. 9, Art. no. 2101043, 2021, doi: 10.1002/adom.202101043.

[21] S. Liu, Y. Ma, J. Wang, R. Sui, and D. Feng, "Multifrequency time modulation for harmonic energy redistribution using metasurfaces," *IEEE Trans. Antennas Propag.*, vol. 73, no. 11, pp. 9345–9354, 2025, doi: 10.1109/TAP.2025.3594535.

[22] T. T. Koutserimpas, F. Monticone, and C. Valagiannopoulos, "Extreme frequency selectivity by synchronized time-modulated metasurfaces," *Scientific Reports*, vol. 15, Art. no. 19023, 2025, doi: 10.1038/s41598-025-00615-0.

[23] D. Yang, A. Das, S. D. Campbell, and D. H. Werner, "Harmonic engineering of antennas with time-periodic substrate permittivity, *Phys. Rev. Applied*, vol. 23, Art. no. 024008, 2025, doi: 10.1103/PhysRevApplied.23.024008.

[24] M. M. Sadafi, A. Fontana da Mota, and H. Mosallaei, "Time-varying Mie resonators for real-time manipulation of quantum emitter radiation, *Phys. Rev. B*, vol. 111, Art. no. 125419, 2025, doi: 10.1103/PhysRevB.111.125419.

[25] T. F. Allard, J. E. Sustaeta-Osuna, F. J. García-Vidal, and P. A. Huidobro, "Broadband dipole absorption in dispersive photonic time crystals, *Phys. Rev. Lett.*, vol. 136, Art. no. 106903, 2026, doi: 10.1103/gttv-6lqc.

[26] J. E. Sustaeta-Osuna, T. F. Allard, F. J. García-Vidal, and P. A. Huidobro, "Near-field gain and far-field control via a plasmonic time crystal slab," *Phys. Rev. Lett.*, vol. 136, Art. no. 136903, 2026, doi: 10.1103/lfr1-dwlv.

[27] D. Globosits, J. Hüpfl, and S. Rotter, "Pseudounitary Floquet scattering matrix for wavefront shaping in time-periodic photonic media," *Phys. Rev. A*, vol. 110, Art. no. 053515, 2024, doi: 10.1103/PhysRevA.110.053515.

[28] B. Vial and R. V. Craster, "Quasinormal modes of Floquet media slabs," *Phys. Rev. B*, vol. 112, Art. no. 214201, 2025, doi: 10.1103/xxnd-7d55.

[29] Y. Sun, S. Fan, and G. Hu, "Quasinormal mode basis for open Floquet photonic systems," *Phys. Rev. Lett.*, vol. 136, Art. no. 206903, 2026, doi: 10.1103/175n-lksd.

[30] A. Canós Valero, S. Gladyshev, D. Globosits, S. Rotter, E. A. Muljarov, and T. Weiss, "Revealing the resonant physics of open photonic time crystals," *Laser & Photonics Reviews*, Art. no. e71318, 2026, doi: 10.1002/lpor.71318.

[31] D. Globosits, P. Garg, J. Hüpfl, A. Canós Valero, T. Weiss, C. Rockstuhl, and S. Rotter, "Exceptional points, lasing, and coherent perfect absorption in Floquet scattering systems," *Light: Science & Applications*, vol. 15, Art. no. 375, 2026, doi: 10.1038/s41377-026-02380-9.

[32] Y. Ren, H. Pan, and J.-S. Wang, "Clarification of Floquet-enhanced thermal emission through the nonequilibrium Green's function formalism," *Phys. Rev. B*, vol. 113, Art. no. 075415, 2026, doi: 10.1103/rm6n-rcxc.